ADVANCED FUNCTIONAL MATERIALS
www.afm-journal.de

Resolving Donor–Acceptor Interfaces and Charge Carrier Energy Levels of Organic Semiconductors with Polar Side Chains

Riccardo Alessandri, Selim Sami, Jonathan Barnoud, Alex H. de Vries, Siewert J. Marrink,* and Remco W. A. Havenith**

Organic semiconductors consisting of molecules bearing polar side chains have been proposed as potential candidates to overcome the limitations of organic photovoltaics owing to their enhanced dielectric constant. However, introducing such polar molecules in photovoltaic devices has not yet resulted in higher efficiencies. A microscopic understanding of the impact of polar side chains on electronic and structural properties of organic semiconductors is paramount to rationalize their effect. Here, the impact of such side chains on bulk heterojunction overall morphology, molecular configurations at donor–acceptor (DA) interfaces, and charge carrier energy levels is investigated. The multiscale modeling approach used allows to resolve DA interfaces with atomistic resolution while taking into account the large-scale self-organization process which takes place during the processing of an organic thin film. The polar fullerene-based blends are compared to the well-studied reference system, poly(3-hexyl-thiophene) (P3HT):phenyl-C_{61}-butyric acid methyl ester (PCBM). Introduction of polar side chains on a similar molecular scaffold does not affect molecular orientations at the DA interfaces; such orientations are, however, found to be affected by processing conditions and polymer molecular weight. Polar side chains, instead, are found to impact considerably the charge carrier energy levels of the organic blend, causing electrostatic-induced broadening of these levels.

1. Introduction

Functionalization of organic semiconductors with polar ethylene glycol (EG) side chains is recently emerging as a key strategy to boost performance in organic electrochemical transistors[1,2] and organic thermoelectric devices.[3–5] In contrast to traditional apolar alkyl side chains, EG side chains have a relatively high degree of polarity due to the permanent dipole moments introduced by substitution of methylene units for oxygen atoms. Replacement of alkyl by EG chains has been found to increase the doping efficiency of organic semiconductors in thermoelectric devices—mostly due to an increased host–dopant miscibility,[3–5] to allow for mixed ionic-electronic conduction,[1,6] to decrease the π–π stacking distance of polymer backbones,[7] and to increase the dielectric constant.[8–11] The increase in the dielectric constant of organic semiconductors has been proposed as a strategy to increase the performance of organic photovoltaics (OPVs).[12] Although EG side chains in particular have found ample use in achieving organic materials with increased dielectric constants,[8–11,13–15] this has not yet resulted in OPV devices achieving higher efficiencies.[14] A microscopic understanding is paramount to rationalize the effect of polar side chains in blends of organic semiconductors. Here, we investigate the impact of introducing polar side chains in bulk heterojunction (BHJ) solar cells by multiscale modeling: We study how their introduction affects phase separation, molecular orientations at the DA interfaces, and charge carrier energy levels.

Dr. R. Alessandri, S. Sami, Dr. J. Barnoud,[+] Dr. A. H. de Vries, Prof. S. J. Marrink, Dr. R. W. A. Havenith
Zernike Institute for Advanced Materials
University of Groningen
Nijenborgh 4, 9747 AG Groningen, The Netherlands
E-mail: ric.alessandri@gmail.com; s.j.marrink@rug.nl; r.w.a.havenith@rug.nl

The ORCID identification number(s) for the author(s) of this article can be found under https://doi.org/10.1002/adfm.202004799.

[+]Present address: Intangible Realities Laboratory, School of Chemistry, University of Bristol, Cantock's Close, Bristol BS8 1TS, UK

Dr. R. Alessandri, Dr. J. Barnoud, Dr. A. H. de Vries, Prof. S. J. Marrink
Groningen Biomolecular Sciences and Biotechnology Institute
University of Groningen
Nijenborgh 7, 9747 AG Groningen, The Netherlands

S. Sami, Dr. R. W. A. Havenith
Stratingh Institute for Chemistry
University of Groningen
Nijenborgh 4, 9747 AG Groningen, The Netherlands

Dr. R. W. A. Havenith
Ghent Quantum Chemistry Group
Department of Inorganic and Physical Chemistry
Ghent University
Krijgslaan 281 (S3), Gent B-9000, Belgium

DOI: 10.1002/adfm.202004799

Despite a growing body of literature comprising modeling studies of organic semiconductors,[16–19] only few of them have considered the impact of the polarity of the side chains on the functioning of organic devices. For example, by comparing C_{60} and C_{70} to their well-known soluble derivatives, phenyl-C61-butyric acid methyl ester (PCBM) and the analogous $PC_{71}BM$, it was found that fullerene functionalization leads to increased energetic disorder in neat fullerene morphologies.[20,21] Fullerene functionalization also decreases the electronic, or high frequency, dielectric constant,[22] with the increased dielectric constant values recorded for (EG-)functionalized fullerenes,[8] which are thus expected to stem from dipolar contributions. The dipolar origin of such contribution was very recently confirmed by polarizable molecular dynamics (MD) simulations, which also highlighted a synergistic effect between the highly polar EG units and the highly polarizable C_{60} which contributes to the increase in dielectric constant.[23] Such dipolar contributions may positively influence the charge separation process in OPV devices. This scenario is supported by the study of de Gier and co-workers,[24] where side chains bearing dipole moments have been shown to positively influence the charge separation by stabilizing the charge separated state relative to the lowest charge transfer state.[24] However, the time scale of the response of such dipoles may not be quick enough to alleviate organic photovoltaics recombination losses.[23] A definitive picture of the overall positive influence of polar side chains in BHJ solar cells has yet to emerge.

EG-functionalization may also influence molecular configurations at the DA interfaces. Such configurations have been linked to organic solar cell device performance in several studies, both theoretically and experimentally.[25–30] Experimentally, while some information regarding molecular configurations at the interfaces can be obtained for planar heterojunctions,[25,26,30] few studies obtained such information for BHJ interfaces,[27,28] and there is no wide-spread method to characterize preferential orientation at the DA interfaces in BHJs. Despite the potential of computational modeling to help in this endeavour, previous work was limited either by too low molecular resolution—which makes a direct link to molecular configuration ambiguous,[31–33] or by timescales—which lead to the modeling of pre-assembled interfaces, thereby hampering the prediction of relative abundance of DA configurations in a given blend.[29,34,35]

In what follows, we resolve molecular configurations at the DA interface of realistic[36] BHJ morphologies while taking into account the large-scale self-organization process which takes place during the processing of an organic thin film. A detailed configurational analysis shows how structures at the DA interface are affected by the molecular weight of the polymer—poly(3-hexyl-thiophene) (P3HT)—and processing conditions such as thermal annealing. In the case of the reference P3HT:PCBM blends, while low-molecular-weight P3HT leads to more end-on DA configurations, higher-molecular-weight P3HT is found to promote face-on configurations. We then investigate the impact of polar EG-based side chains by replacing the reference fullerene derivative PCBM with a recently synthesized fulleropyrrolidine which showed[8] an enhanced dielectric constant—PTEG-1. We study how a higher degree of polarity affects 1) the phase separation, 2) the relative orientations of the donor and acceptor molecules at DA interfaces, and 3) the charge carrier energy levels. Functionalization of the fullerene acceptor by EG side chains is found to impact the phase separation to a minimal degree in this case, and it does not impact molecular orientations at the DA interfaces. In contrast, the permanent dipoles of the polar side chains have a large impact on the energetics of the organic blend. Microelectrostatic calculations predict that installing polar side chains leads to considerable broadening of the charge carrier energy levels, due to increased electrostatic disorder.

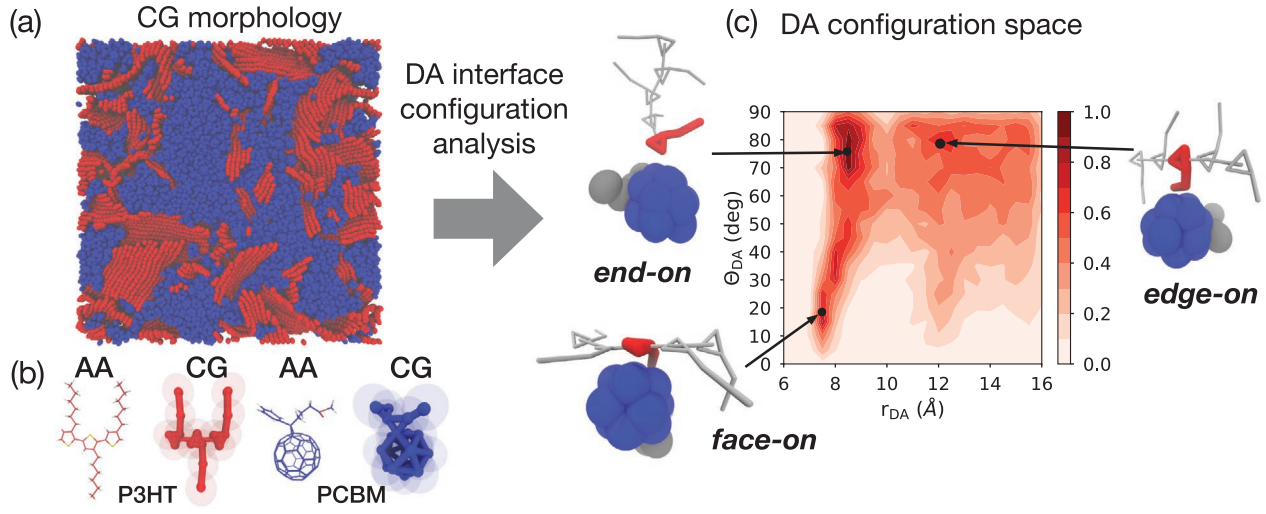

Figure 1. Molecular configurations at donor–acceptor interfaces of simulated P3HT:PCBM morphologies. a) Morphology of a blend of P3HT (24-mer) and PCBM at CG resolution generated via solvent evaporation simulations. b) All-atom (AA) and CG representations of a P3HT (for clarity, a trimer is shown) and a PCBM molecule. c) DA configurational space, obtained by partitioning all of the DA pairs at the DA interfaces of a given morphology in the 2D space formed by the distance, r_{DA}, connecting the center of mass of C_{60} and the center of mass of the thiophene ring, and the angle, θ_{DA}, between the r_{DA} vector and the vector normal to the thiophene plane. In this way, regions in the 2D map represent the different DA molecular configurations: face-on, end-on, and edge-on (see insets). In the insets, the reference P3HT monomer and C_{60} fullerene are highlighted in red and blue, respectively; neighboring P3HT monomers and PCBM side chains are shown in gray. Note that P3HT chains are not rendered in full—only five consecutive monomers are shown—for clarity.

2. Results and Discussion

2.1. Molecular Configurations at Donor–Acceptor Interfaces

We first characterize structurally the DA interfaces in the reference P3HT:PCBM system. We generate realistic BHJ morphologies at the coarse-grain (CG) level (**Figure 1**a) via large-scale solvent evaporation MD simulations (see the Experimental Section).[31,36] Such simulations mimic the solution-processing step through which organic thin films are produced experimentally, and were previously shown to lead to morphologies in agreement with experimental scanning electron microscopy and scattering data.[36] The use of Martini[37,38] CG models, which retain a sizable degree of chemical specificity and structural detail (Figure 1b), allows for direct analysis of the DA interfaces of such CG morphologies: we thus retrieve (see Experimental Section) maps of the relative abundance of different DA molecular orientations (Figure 1c).

A representative map for a simulated solution-processed P3HT:PCBM blend (P3HT molecular weight of 2 kDa) is shown in Figure 1c. The map gives a view on the relative abundance of DA configurations found at the heterointerfaces of the blend, which can be classified—according to the relative position and orientation of the donor and acceptor π-systems[29,39]—in three categories: face-on, end-on, and edge-on. These categories apply in the case of an isotropic shape for one of the two molecules of the blend—this being the case of, for example, fullerene-based organic mixtures. Characteristic snapshots of such configurations are shown as insets in Figure 1c for the P3HT:PCBM blend: in face-on configurations, the P3HT thiophene rings face C_{60}; in end-on configurations, the P3HT thiophene rings are in contact with C_{60} but the normal to their plane is oriented perpendicularly to the C_{60}–thiophene connecting vector (such a configuration can occur with a P3HT thiophene which is at either of the two ends of a P3HT molecule); finally, in edge-on configurations, P3HT side chains separate C_{60} and the π-system of P3HT.

The map of Figure 1c shows examples of these three configurations, as three regions can be distinguished. In the bottom-left corner, we can individuate face-on configurations, since such configurations imply the shortest possible r_{DA} distance and a $\theta_{DA} \approx 0°$ ($r_{DA} \approx 7.5$ Å, $0° \leqslant \theta_{DA} < 25° \Rightarrow$ face-on). In the top-left corner, we can locate end-on configurations, since such configurations imply a slightly larger r_{DA} distance and a $\theta_{DA} \approx 90°$ ($r_{DA} \approx 8.5$ Å, $65° < \theta_{DA} \leqslant 90° \Rightarrow$ end-on). Finally, around the same angle, but at a larger distance, we can individuate edge-on configurations ($r_{DA} \approx 12$ Å, $65° < \theta_{DA} \leqslant 90°$, $\Rightarrow$ edge-on). The map indicates that, not surprisingly, multiple type of DA interfaces coexist in BHJs. In the next section, we will thoroughly investigate some factors which can affect the relative abundance of molecular configurations at the heterointerfaces.

2.2. Effect of Polymer Molecular Weight and Thermal Annealing on Configurations at Interfaces

Both P3HT molecular weight (MW) and thermal annealing—a process often employed to post-process solution-processed organic thin films—are known to affect the structural organization of P3HT:PCBM blends on the mesoscale. In particular, low-MW P3HT is known to crystallize more readily,[40,41] while in the case of many OPV blends, both fullerene-based[42] and nonfullerene-based,[43] annealing the organic film boosts the performance of the device considerably. Annealing is known to increase the crystallinity of (at least) one of the two components of typical organic blends.[42,43] As a consequence, phase separation also usually increases. However, it is not clear whether and how these two "parameters"—the MW of the polymer phase and thermal annealing—impact the molecular configurations at the DA interfaces. We thus performed the configurational analysis of P3HT:PCBM blends at various P3HT MWs and before and after thermal annealing.

We first discuss the results obtained as a function of P3HT MW. We vary the MW of P3HT from 2 to 8 kDa, corresponding to P3HT chains that are 12 to 48 monomers long. **Figures 2**a and 2c show typical snapshots of as-cast and annealed (see below) P3HT:PCBM blends for P3HT MW of 2 and 8 kDa, respectively. Their corresponding DA configuration phase spaces are shown in Figure 2b and 2d, respectively. Comparing the DA phase spaces, the first clear feature is the enrichment in end-on configurations of the low-MW blend, while the high-MW blend is dominated by face-on configurations. This may be understood in terms of the face/end ratio of the two different P3HT chain lengths: Low-MW P3HT contains more chain-ends than high-MW P3HT; thus, there is less P3HT "face" available for fullerenes to dock in the low-MW case. A second feature is the more marked region at larger r_{DA}, corresponding to edge-on configurations, in low-MW blends. Results for more blends, including intermediate MWs, are shown in Figure S1, Supporting Information, and confirm the trends just described: As the P3HT chain length increases, the dominant DA configuration shifts from end-on to face-on.

We anneal the simulated as-cast BHJs (as recently done in ref. [36]—see also Experimental Section) and perform the DA configuration analysis on the resulting morphologies. Comparing the annealed blends and corresponding DA configuration maps of Figure 2 to their as-cast counterparts, we note a few differences between the two extremes of the range of MWs studied here upon thermal annealing. In the low-MW case, the crystallinity of the P3HT phase increases dramatically, as can be qualitatively seen from Figure 2 and as shown in previous work.[36] The enhanced crystallinity has two consequences on the DA configurations: i) an even more drastic shift towards end-on orientations, and ii) the disappearance of the population at larger distances, due to the formation of contacts between side chains of different P3HT molecules upon P3HT lamella formation. This lamella formation reduces the surface of free P3HT side chains which can be approached by fullerene molecules, hence decreases the DA population on the top-right corner of Figure 2b. However, in the high-MW case, the dominant configuration remains face-on, and only a little decrease in the edge-on population is noticeable. This again can be rationalized by considering the different face/end ratio of P3HT chains; this time considering also the effect of annealing, that is enhanced crystallinity. In the low-MW annealed case, P3HT backbones readily come together to form polymer crystallites, leaving even fewer backbone "faces" free for interactions with the fullerene. At the same time, the "end" of the crystal grows, effectively increasing the "end-on surface" available for the fullerene derivatives to dock, and hence, the further increase of the end-on feature of the 2D map. Also, fewer side chains are free due to the growth of P3HT lamella upon crystallization, thus

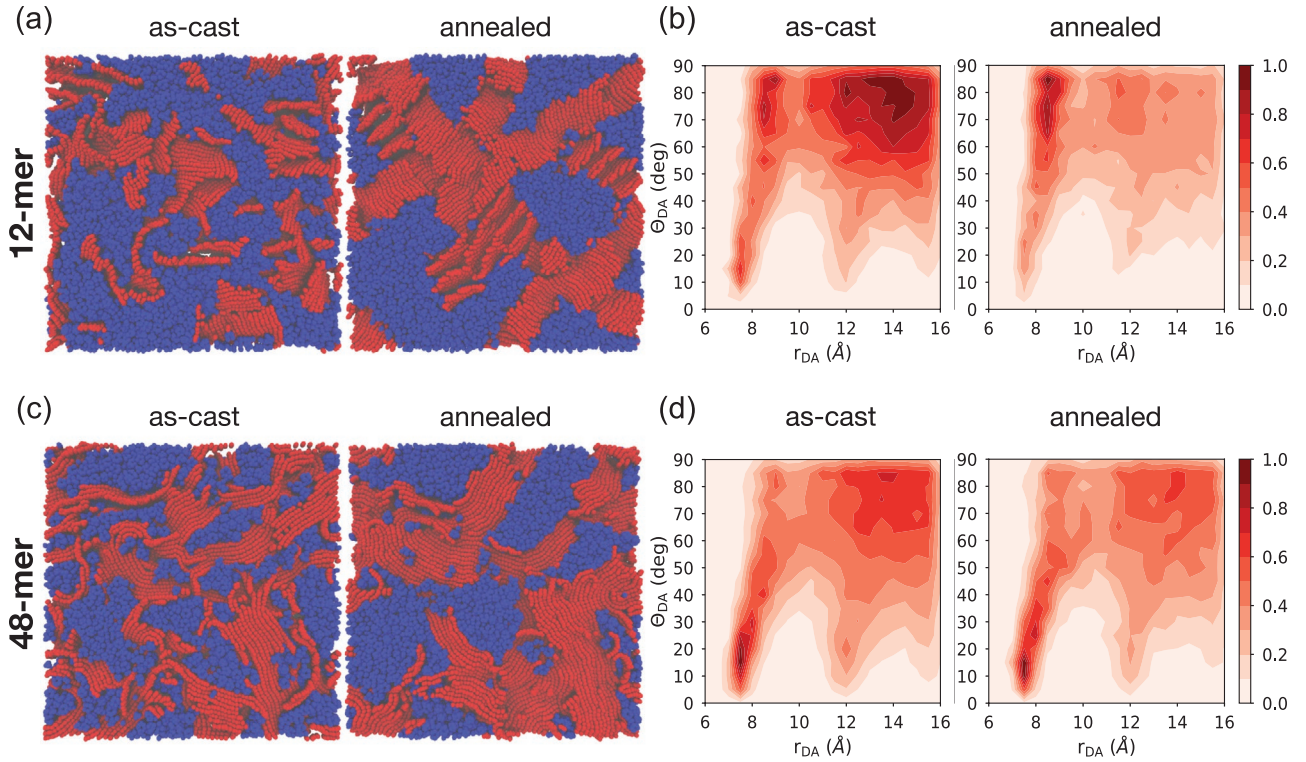

Figure 2. Effect of molecular weight and thermal annealing on the donor-acceptor configurations at the interfaces of P3HT:PCBM blends. Renderings of as-cast and annealed simulated bulk heterojunctions are shown for a) low MW (2 kDa, corresponding to a 12-mer) and c) high MW (8 kDa, corresponding to a 48-mer) P3HT blends. Their corresponding DA configuration phase spaces are shown in b) and d), respectively. Upon increasing P3HT MW, configurations at DA interfaces shift from end-on enriched to face-on dominated. Upon annealing, the enhanced crystallinity of the P3HT phase leads to an even more drastic shift to end-on configurations for low MW blends (c), while has little effect on the high MW blend (d). In (a) and (c), P3HT side chains are not rendered to highlight the organization of P3HT backbones; plot in (b) and (d) are normalized to the total number of DA pairs.

decreasing the "edge-on surface" as well. In the heaviest-MW case, the impact of annealing is relatively reduced with respect to the low-MW case—in agreement with earlier results[36] and experiments which show a higher sensitivity of low-MW P3HT to processing conditions[41]—showing only a minor decrease in the edge-on population. The dominant interface configuration remains face-on.

Given the fact that the heaviest P3HT studied here is still lighter than the ones employed in P3HT-based OPV devices (8 vs 30–60 kDa[44]), the picture derived in the highest MW case is likely to be more relevant than the low MW one for actual P3HT solar cells and, in general, for polymer-based blends. In contrast, the low-MW P3HT picture which emerges is likely to be relevant for small-molecule-based[45] organic blends.

These findings indicate also that the ratio between the multiple pathways through which charge separation occurs within a BHJ[29,35] may change depending on the P3HT MW and processing conditions. In particular, Fazzi et al. have recently reported[46] that end-on configurations allow for "cold-splitting" of excitons,[47] where intermediate charge-transfer states first thermalize and then split intro free charges; in contrast, face-on configurations are more suited to a "hot" charge separation mechanism,[48] where the excess vibrational energy of the higher lying intermediate charge-transfer state is used to overcome the Coulomb attraction between the hole and the electron. In view of the present work, high MW P3HT:PCBM blends are expected to allow for cold exciton splitting to a lesser degree than low MW ones, given the dominance of face-on configurations at the heterointerfaces. In the present case, shifts on the DA configuration populations at the heterointerfaces are driven by the chain length and degree of crystallization of the polymer. However, other factors such as sterical accessibility of molecular moieties[49] may also play a role. The current protocol allows to explore whether and to which extent factors such as processing conditions and molecular features impact the relative orientations of molecules at the DA interfaces. This constitutes a necessary step in the direction of an increased rational approach to the design of high performance OPVs.

2.3. Impact of Polar Side Chains on the Phase Separation and DA Configurations

We now investigate the impact of polar side chains in bulk heterojunctions, first from a structural point of view. To this end, we replace the reference fullerene derivative, PCBM, with a recently synthesized[8] fulleropyrrolidine, PTEG-1 (**Figure 3**e). PTEG-1 has a longer and EG-based side chain and showed a dielectric constant of 5.7 ± 0.2, considerably higher than the one of the reference compound PCBM (3.9 ± 0.1).[8]

Figure 3 collects a structural comparison between P3HT-based blends of the two fullerene derivatives, PCBM and PTEG-1 (see Figure 3a,e for the atomistic structures and CG

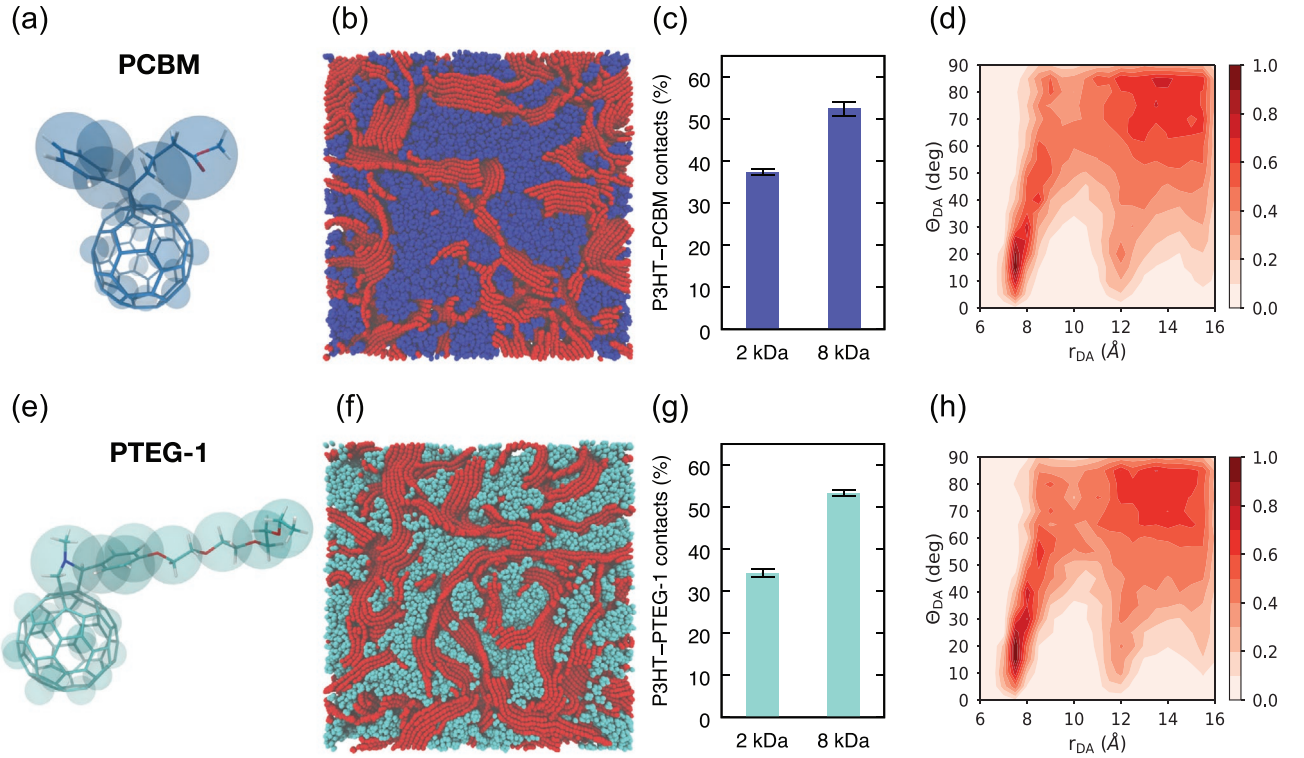

Figure 3. Structural impact of polar side chains. a–d) P3HT-based blends of the reference fullerene derivative PCBM are compared to e–h) P3HT-based blends of PTEG-1, a fullerene derivative bearing an EG-based polar side chain (see (e) for a rendering of its atomistic structure overlaid with its CG representation). Snapshots of as-cast b) P3HT:PCBM and f) P3HT:PTEG-1 simulated BHJs are shown for the 8 kDa P3HT case. In this case, polar side chains tend to slightly increase the miscibility between the donor and acceptor molecules, as quantified by the number of DA contacts for the c) P3HT:PCBM and g) P3HT:PTEG-1 blends. DA configurations at the interfaces—shown in (d) and (h) for 8 kDa P3HT-based blends—show, however, no major difference.

representations of the two fullerene derivatives). We first analyze the impact of the EG-based side of PTEG-1 on the overall phase separation. We do so by looking at the number of donor–acceptor contacts throughout the simulated BHJ: a higher number of such contacts indicates higher likelihood to find a P3HT molecule close to a fullerene one, i.e., a more intimately mixed morphology. The numbers of contacts in the planar heterojunction and completely intermixed extremes, respectively, have been used as references to normalize the computed fraction of P3HT-fullerene contacts (see also ref. [36] and Figure S4, Supporting Information). While low P3HT MW blends show slightly decreased mixing upon EG-functionalization of the fullerene (Figure 3c,g, 2 kDa), high P3HT MW blends show no significant difference in mixing (Figure 3c,g, 8 kDa), as quantified by the number of P3HT-fullerene contacts in the two cases. A larger difference in polarity between P3HT and PTEG-1 may explain the decreased mixing in the low MW blends. However, overall the predicted effect on the morphology phase separation is minimal.

Turning to the DA interfaces, representative 2D maps of the DA configuration spaces are shown in Figure 3d,h. They show no major difference between P3HT:PCBM and P3HT:PTEG-1 blends (see also Figure S2, Supporting Information). Accordingly, we conclude that the overall geometry of the molecules, that is C_{60}-like in the case of both PCBM and PTEG-1, drives molecular orientations at the DA interfaces, and dominates over side chain functionalization with ethylene glycol. Sizable differences are expected in the case of going from fullerene to non-fullerene acceptors, given the anisotropic shape of the latter. This is currently being investigated and will be part of future work.

2.4. Effect of Polar Side Chains on the Charge Carrier Energy Levels

We now turn to explore the impact of polar side chains on the charge carrier energy levels of bulk heterojunctions. The CG morphologies are thus backmapped—using a published protocol[50] (see Experimental Section)—to retrieve full atomistic resolution. Subsequently, we compute hole and electron energy levels, ionization potentials (IPs), and electron affinities (EAs), for the simulated BHJs. We employ tight-binding density functional theory (DFTB)—see also the Experimental Section—to compute the gas-phase energy levels. In condensed phases, charge carrier energy levels are largely affected by intermolecular interactions. These shift the gas-phase IP and EA values,[51] and stabilize charges with respect to the gas-phase. Such shifts are called polarization energies and are usually indicated as P^+ for a hole, and P^- for an electron. Two main contributions determine $P^{\pm}$[51]: 1) the contribution of the electrostatic field experienced by the charge carrier in the condensed phase—the electrostatic contribution, $S^{\pm}$; and 2) the contribution of the induced dipoles between the charge carrier and its surrounding—the induction contribution, $I^{\pm}$. We evaluate these two contributions and hence the polarization energies by microelectrostatic, or induced dipoles, calculations using the

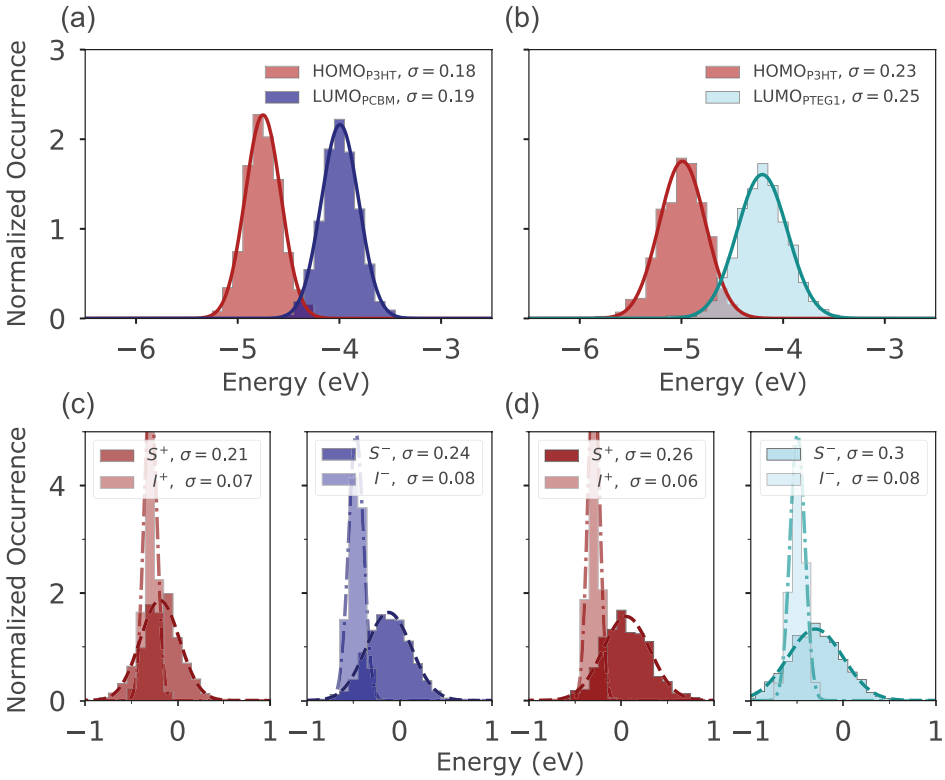

Figure 4. Impact of polar side chains on the charge carrier energy levels of simulated bulk heterojunctions. Charge carrier energy levels in a) P3HT:PCBM and b) P3HT:PTEG-1 blends: the introduction of polar side chains broadens the hole and electron energy levels in the BHJ, with standard deviations (σ) which increase from 0.18 and 0.19 eV for the hole and electron energy levels in P3HT:PCBM blends to 0.23 and 0.25 eV in P3HT:PTEG-1 ones. c,d) The decompositon of the energy distributions in electrostatic, $S^{\pm}$, and induction, $I^{\pm}$, contributions, highlights that the increased broadening is due to increased electrostatic disorder caused by the presence of the dipole-loaded EG side chains.

classical polarizable direct reaction field (DRF) force field as implemented in the DRF90 software.[52] We consider a central molecule—either neutral or charged—and a surrounding of 2 nm around such molecule taken from the simulated large-scale morphology (for details, see the Experimental Section).

P3HT-based BHJs containing PTEG-1 lead to broader charge carrier energy level distributions, as shown in **Figure 4**. The standard deviation (σ) of these distributions quantifies the energetic disorder. Both the HOMO and LUMO energy distributions are considerably broader in blends containing PTEG-1. In particular, σ increases on average by 30% when going from P3HT:PCBM to P3HT:PTEG-1 blends, indicating increased energetic disorder. It is instructive to first compare the electron energy levels in neat fullerene morphologies of PCBM and PTEG-1, as shown in **Figure 5**. While the gas-phase LUMO levels almost coincide (Figure 5a), once the electrostatic and induction effects of the surrounding molecules are taken into account, the LUMO distributions broaden considerably, and this is more so in the case of PTEG-1. For PCBM, $\sigma = 0.22$ eV, a value somewhat higher than the ones reported in previous computational works (0.13[20] and 0.17 eV[21]), which is due to a difference in the magnitude of the induction contribution when comparing to ref. [21] (see below). As compared to PCBM, PTEG-1 shows a markedly broader distribution, with $\sigma = 0.30$ eV.

Analyzing the contributions to the broadening of the energy levels, Figure 5b shows that: 1) the energetic disorder is mostly due to the electrostatic contribution, in agreement with previous findings[21]; the $\sigma_{S^-} = 0.28$ eV obtained for PCBM agrees well with the value obtained by D'Avino et al.[21]; 2) the induction contribution is the same in both cases; this is not surprising, as the polarizability of PCBM and PTEG-1 are expected to be very similar given the fact that they are dominated by C_{60}; we note also that the induction contribution is about half in magnitude than what computed by D'Avino et al.,[21] which explains the discrepancy in the total σ for PCBM between this work and ref. [21]; the difference is likely due to such contribution being extrapolated for an infinite crystal in ref. [21] while here a 2 nm cutoff is used; 3) the induction contribution is anti-correlated with the electrostatic one (Figure S7, Supporting Information): as a consequence, the final energetic disorder is smaller when considering the induction than what it would be in a purely electrostatic picture—in agreement with previous findings[21]; given the underestimation of the induction contribution in this work with respect to ref. [21], this may translate into an overestimation of the obtained total energetic disorders; however, given that the induction contribution is mostly due to C_{60} fullerene, no qualitative effect is expected on the relative difference between the PCBM- and PTEG-1-based systems; 4) the electrostatic contribution is centered around zero for PCBM but has an overall stabilizing effect in the case of PTEG-1: this indicates that the combination of the arrangements of PTEG-1 molecules and its dipoles, along with the localization of the excess charge, gives rise to favorable

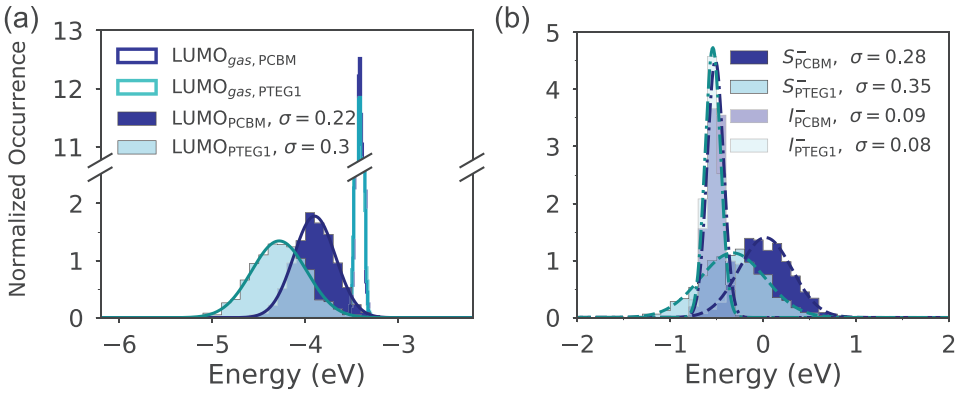

Figure 5. Electron energy levels in neat fullerene morphologies: PCBM versus PTEG-1. The gas-phase LUMO levels (computed at the DFTB level, and with $\sigma = 0.03$ eV for both PCBM and PTEG-1) broaden in the condensed phase, leading to LUMO energy distributions with standard deviations of 0.22 and 0.30 eV for PCBM and PTEG-1, respectively. On the right-hand side, we analyze the total P^- by decomposing into the electrostatic, S^-, and induction, I^-, contributions. The S^- is mostly responsible for the broadening of the LUMO energy distributions. The I^- compensate slightly for the electrostatic-induced broadening, leading to a reduction of the 0.28 and 0.35 eV standard deviations of the S^- distributions to the 0.22 and 0.30 eV standard deviations of the P^- and gas-phase contributions.

interactions. The same effects observed for the neat fullerene morphologies can be observed for the blends (Figure 4); however, this time not only on the electron but also on the hole energy levels, with computed σ's which increase from 0.18 and 0.19 eV for the hole and electron energy levels in P3HT:PCBM blends to 0.23 and 0.25 eV in P3HT:PTEG-1 ones. It should be noted that these numbers should be compared to microscopic σ values, that is, values of σ obtained with microscopic modeling techniques such as the microelectrostatic calculations used here, which are usually larger (i.e., 100–180 meV[21,53]) than the σ values obtained by fitting experimental data to lattice models (i.e., 70–150 meV[53–55]) such as the extended correlated Gaussian disorder model (ECDM).[54] This difference is due to assumptions included in the analytical expressions of lattice models which might not hold for the microscopic models.[53] The range of σ's obtained for P3HT:PCBM blends are in line with, if not slightly larger than, previously reported microscopic σ's, while the values obtained for P3HT:PTEG-1 blends exceed the "common" range and exhibit strong energetic disorder. We note also that an increase in energetic disorder caused by polar side chains has been also computationally observed in columnar discotic liquid crystals.[56] In conclusion, the longer and dipole-loaded side chain of PTEG-1 gives rise to considerably more electrostatic disorder, which broadens both charge carrier energy levels.

According to the present findings, we speculate that PTEG-1 is predicted to decrease the open-circuit voltage (V_{OC}), given the same blend, due to increased electrostatic-induced disorder of the interfacial energy levels.[57] Such a decrease in V_{OC} was previously reported upon EG-functionalization of polymers[7] and nonfullerene acceptors,[58] and upon cyano-functionalization[59] of polymers, the latter being another way of introducing permanent dipole moments in organic semiconductors.[14] Broadening of charge carrier energy levels can also lead to lower mobilities.[59] A decrease in V_{OC} and lower charge carrier mobilities are detrimental to the efficiency of OPVs. However, polar side chains may counterbalance this detrimental effect by stabilizing charge separated states,[24] thereby making the charge dissociation more enthalpically favorable, or by suppressing bimolecular recombination. Indeed, other factors such as an increased CT state lifetime or a decreased CT state binding energy can positively influence the V_{OC},[57] which may explain why PTEG-1 was found to have a larger V_{OC} when blended with the polymer PTB7 than PCBM.[60]

3. Conclusion

We investigated the effect that functionalization of an organic semiconductor with polar side chains has on the structural and energetic landscape of organic blends. The multiscale modeling approach used allows for the investigation of molecular orientations at the heterointerfaces as a function of processing conditions and molecular features. In general, low-molecular-weight P3HT is found to lead to more end-on donor–acceptor configurations, while higher-molecular-weight P3HT is found to promote face-on configurations. The impact of a polar fullerene derivative on phase separation and donor–acceptor configurations is only limited. However, the dipole-loaded side chains of the polar fullerene impact considerably the charge carrier energy levels. They induce broadening of the latter by electrostatic disorder. This may be undesirable, as it leads to charge carrier relaxation, which in turn can lead to lower charge mobilities and voltage losses.

The polar side chain-induced broadening of charge carrier energy levels is not restricted to fullerene-based organic solar cells but is expected to be relevant for all molecular semiconductors and thus is anticipated to play a similar role also in nonfullerene-based or all-polymer organic solar cells.

4. Experimental Section

Coarse-Grain and Atomistic Models: CG models based on the Martini force field were used.[37,38] The models for P3HT and PCBM were taken from ref. [36], while the model for PTEG-1 from ref. [61]. The PTEG-1 model uses the latest EG Martini parameters[62] which are the most transferable EG parameters within the current version of the Martini force field (EG notably making for a difficult modeling case in Martini partly because it requires a three-to-one atoms-to-bead

mapping[63]). The Martini C_{60} model was developed in ref. [64]. Refer to these publications for a thorough description of the models and their validation. Atomistic models were built upon the models developed in refs. [36,61]. Nonbonded parameters were taken from the GROMOS 53A6 force field.[65] Bonded parameters, however, were derived from quantum chemical (QC) calculations using the Q-Force toolkit (see Supporting Information). Compared to general atomistic molecular mechanics force fields which use libraries of bonded parameters to enhance transferability, the Q-Force approach derives molecule-specific bonded parameters, and has thus the benefit of having an MD potential energy landscape matching the QC one. This is highly beneficial for later performing QC calculations on geometries obtained from MD simulations, as the use of general force field geometries for QC calculations may lead to systematic and/or uncontrolled errors.[17,66] The Q-Force procedure used in this work consisted of two steps: i) fitting of the stiff bonded force field terms (bonds, angles, stiff dihedrals, and improper dihedrals) to the QC Hessian and ii) fitting of the flexible EG dihedral potentials to the ωB97X-D[67]/6-311G(d,p) dihedral scans. These two steps are further explained in Supporting Information. There, the effect of using GROMOS and Q-Force bonded parameters on QC energies is also compared (see also Figure S6 and associated discussion, Supporting Information). A script to generate arbitrarily long all-atom P3HT chains and their corresponding GROMACS topology files has been developed and can be downloaded from Figshare.[68] Details on the script are given in Supporting Information.

Simulated Solvent Evaporation and Thermal Annealing: Morphologies were generated by solvent (the solvent being chlorobenzene, CB) evaporation MD simulations as in ref. [36], following the method introduced by Lee and Pao.[31] More specifically, starting from a simulation box ($30 \times 30 \times 88$ nm^3) containing a ternary mixture P3HT:fullerene:CB (with fullerene being either PCBM of PTEG-1) in a 1:0.8 weight ratio (corresponding to concentrations of ≈39 mg mL^{-1} in P3HT and ≈31 mg mL^{-1} in PCBM), 1.25% of CB was removed every 15 ns until a dried blend was obtained ($30 \times 30 \times 5$ nm^3). This led to a total drying time of 11 µs, which was found to lead to morphologies in agreement with experimental scanning electron microscopy data.[36] For further details, refer to ref. [36]. The code used for the evaporation is available at https://github.com/ricalessandri/evaporate. Run parameters in the CG simulations follow the "new" Martini set of run parameters[69] and are available on the Martini portal http://cgmartini.nl. Simulated thermal annealing was carried out according to ref. [36]. Briefly, the final configuration of a solvent evaporation simulation was annealed by running MD simulations at a higher temperature, as follows: 20 ns at 398 K, 20 ns at 498 K, 160 ns at 598 K, and 1.8 µs at 698 K, totaling to 2 µs of annealing time. The blend was then cooled down by performing 400 ns of MD simulation at 298 K. Note that, while the employed annealing temperature was higher than the experimental one (≈420 K),[44] annealing time scales were also different (blends were commonly annealed for 5–10 min)[44]; this makes a direct comparison between CG and experimental conditions not trivial. The GROMACS package version 2016.x (or later)[70] was employed to run the simulations. The (CG and backmapped) morphologies, as well as the CG and AA topologies (in GROMACS format) and the mapping files, can be downloaded from Figshare.[71]

Backmapping: The procedure developed by Wassenaar et al. was used for converting the CG morphologies back to full atomistic detail.[50] Refer to the publication in ref. [50] for all the details. Briefly, after the initial projection made by the program backward.py through which atoms are placed according to the CG particles-space definitions contained in mapping files, a series of energy minimizations and MD simulations was carried out until a relaxed atomistic morphology was obtained. Further details, including the creation of mapping files, are given in Supporting Information.

Definition of Donor–Acceptor Pairs and DA Configuration Analysis: The determination of the configuration phase space spanned by DA complexes at the interfaces was done at the CG level. No essential information was left out as compared to using the backmapped morphologies, as the analysis was performed using the centers of mass of molecular moieties, such as the center of mass of C_{60}. The implemented procedure consisted of the following four steps—illustrated here for the P3HT:PCBM case, but valid also for P3HT:PTEG-1 blends:

i) Selection of molecules at the DA interface: The CG morphology (typical sizes of $300 \times 300 \times \approx 50$ Å^3) was divided, in the x and y dimensions, in overlapping voxels of dimensions $20 \times 20 \times z$ Å^3; this was done so that no interfaces were missed. Within each voxel, P3HT (PCBM) atoms were then selected if they were found to be within 6 Å of PCBM (P3HT) atoms. These lists were then corrected for double-counting of atoms and complemented with the atoms which were not found to be within the 6 Å but which belong to molecules which had some atoms within the 6 Å.
ii) Reduction of coordinates: The position of the centers of mass of P3HT thiophene rings, PCBM C_{60}s, P3HT side chains, and PCBM side chains were then stored in matrices. Distance matrices between each of these groups were then computed, giving rise to a set of distances which could be used to characterize the DA pairs.
iii) Definition of DA pairs: Iterating over the PCBM molecules at the interfaces, 3HT monomers were considered to form a DA pair if r_{DA}, that is, the C_{60}-thiophene distance, was within a cutoff of 16 Å. For each DA pair, the angle (θ_{DA}) between the vector normal to the thiophene plane ($\vec{r}_{THIO}$) and the vector connecting the center of mass of the C_{60} and the center of mass of the thiophene ring ($\vec{r}_{DA}$) was computed, another geometrical feature characterizing the DA pair along with the distances computed in step (ii).
iv) Projecting the DA phase space on selected coordinates: The DA pair phase space was then projected onto the 2D space formed by the r_{DA} distance and the θ_{DA} angle by binning each DA pair according to their (r_{DA}, θ_{DA}) values. Such 2D projection allowed to distinguish between face-on, edge-on, and end-on DA arrangements. For more details, see Figure S3, Supporting Information.

The whole procedure is implemented in Python and makes extensive use of the MDAnalysis library.[72,73]

Tight-Binding Density Functional Theory Calculations: To compute gas-phase energy levels, self-consistent charge density functional tight binding (SCC-DFTB) was employed[74]—here referred to simply as DFTB. Calculations were performed using the ADF 2016,[75,76] suite of programs, employing the QUASINANO 2015 parameter set.[77] The HOMO and LUMO energy levels of neutral species were computed. Note that, within DFTB, the IP (computed as $U^+ - U^0$ where U^+ and U^0 are the energies of the cationic and uncharged species, respectively) equals the negative of the HOMO energy, while the EA (computed as $U^0 - U^-$, where U^0 and U^- are the energies of the uncharged and anionic species, respectively) equals the negative of the LUMO energy. Moreover, Mulliken charges computed at the DFTB level were employed to capture the conformation-dependent hole (de)localization of P3HT chains (see below). Being about three orders of magnitude faster than DFT, the method allowed for the computation of the gas-phase energy levels for all the molecules of the simulated BHJs (typically between ≈1800 and ≈2400 molecules, totaling $\approx 0.5 \cdot 10^6$ atoms) in about 15 min. A detailed description of the computational cost of the whole methodology is available in Supporting Information.

Microelectrostatic Calculations: The polarization energies on the charge carrier energy levels by an induced dipole (or microelectrostatic) scheme (see refs. [51,78] for recent reviews) were computed. The general framework and the key points and parameters of the approach are briefly summarized here. The polarization energy for a positive or negative charge carrier in a molecular condensed phase is defined as the difference between the values of the ionization potential or electron affinity in the condensed (IP or EA) and gas (IP_{gas} or EA_{gas}) phase[51,79]:

$$P^+ = IP - IP_{gas} \quad (1)$$

$$P^- = EA_{gas} - EA \quad (2)$$

Note that a negative $P^{\pm}$ value stabilizes the charge carrier in the crystal. Note that the historical[51] name of $P^{\pm}$, that is, polarization energies, may

be misleading. Indeed, the $P^{\pm}$ which shift IP_{gas} and EA_{gas} of Equations (1) and (2) have at least two main contributions due to intermolecular interactions: 1) the electrostatic contribution, $S^{\pm}$; and 2) the induction, $I^{\pm}$. Charge delocalization and an intramolecular contribution due to the geometrical relaxation upon ionization do impact $P^{\pm}$ to a lower extent.[51] Thus, $P^{\pm} = S^{\pm} + I^{\pm}$.[51,78]

Here, $S^{\pm}$ and $I^{\pm}$ were computed using the classical polarizable direct reaction field (DRF) force field as implemented in the DRF90 software.[52] The molecules are thus described classically with point charges and atomic polarizabilities. Within DRF, polarizabilities are described according to Thole's method for interacting polarizabilities,[80,81] which avoids numerical instabilities by employing a distance-dependent damping function. The induction contribution has to be evaluated self-consistently.[51,52] In practice, the polarization energy (for a spherical cluster of N molecules) can be obtained with the following expression[78,82]:

$$P_N^{\pm} = U_N^{\pm} - U_N^0 \tag{3}$$

where U_N^0, U_N^+, and U_N^- are the energies of a cluster of N molecules where the central molecule is either neutral, positively, or negatively charged, respectively. The method was first applied to the anthracene crystal—a system widely studied in the literature—and found to give results in line with previous experimental and theoretical data, as shown in Figure S10 and Table S4, Supporting Information. A cutoff of 2 nm was chosen for the microelectrostatic calculations, which corresponded to taking into account the 550–750 molecular groups (where by molecular groups here indicate either a PCBM or PTEG-1 molecule or a P3HT monomer) which were found within 2 nm of a P3HT 12-mer chain. This size for the environment was what was computationally feasible on this scale also given the number of such calculations which have to be performed (namely, between approximately 4500 and 6000 for each morphology sample).

The input of DRF90 requires atomic polarizabilities and atomic charges for each (neutral and charged) molecule. In the case of fullerenes, molecular geometries of the neutral and negatively charged fragments were first optimized at the B3LYP/6-311G(d,p) level of DFT. For both the neutral and anionic fullerene molecules, charge distributions were computed at their respective optimized geometry via the CM5[83] scheme, which was based on Hirshfeld partitioning[84] of the electron density, as implemented in Gaussian 16.[85] Charges were computed with a few basis sets and DFT functionals, among which ωB97XD, and were found to be very robust (see also Supporting Information), in line with previous reports.[83] In the case of P3HT, molecular geometries of neutral P3HT chains with 6, 8, 10, and 12 monomers were first optimized at the ωB97XD/6-311G(d,p) level. CM5 charges for the neutral fragments were then computed as done in the case of the fullerenes. By comparing the charges of these four chains, charges for arbitrarily long neutral P3HT chains were derived. Two types of monomers were distinguished: termini (the two termini 3HT residues) and central (all the monomers but the two termini). For details, refer to Supporting Information. The charges for the positively charged P3HT chains, however, cannot be computed for a single chain conformation, as the flexibility of P3HT chains affects the localization of the hole.[35,86] In order to take into account this dependence of the hole localization on conformational disorder, the approach of D'Avino et al.[35] was followed: Mulliken atomic distributions of excess positive charge for each P3HT geometry at the DFTB level were computed. These were then summed to the CM5 atomic charges of the neutral P3HT, obtaining distributions for charged P3HT chains. The procedure is described in detail in Supporting Information. For the polarizabilities, the standard set of polarizabilities of the DRF force field was employed. These were parametrized on the basis of a large set of experimental molecular polarizabilities.[52,81]

Supporting Information

Supporting Information is available from the Wiley Online Library or from the author.

Acknowledgements

R.A. thanks The Netherlands Organization for Scientific Research NWO (Graduate Programme Advanced Materials, No. 022.005.006) for financial support, and Ria Broer, L. Jan Anton Koster, Piet van Duijnen, Sebastian Thallmair, and Anna S. Bondarenko for stimulating discussions. J.B. was supported by the TOP program of S.J.M., financed by NWO. The research was carried out in affiliation with the FOM Focus Group "Next Generation Organic Photovoltaics" in Groningen. Computational resources for this work were partly provided by the Dutch National Supercomputing Facilities through NWO.

Conflict of Interest

The authors declare no conflict of interest.

Keywords

coarse-graining, donor–acceptor interfaces, multiscale modeling, organic semiconductors, polar side chains

Received: June 5, 2020
Revised: July 27, 2020
Published online: September 6, 2020

[1] A. Giovannitti, D.-T. Sbircea, S. Inal, C. B. Nielsen, E. Bandiello, D. A. Hanifi, M. Sessolo, G. G. Malliaras, I. McCulloch, J. Rivnay, *Proc. Natl. Acad. Sci. USA* **2016**, *113*, 12017.
[2] A. Giovannitti, I. P. Maria, D. Hanifi, M. J. Donahue, D. Bryant, K. J. Barth, B. E. Makdah, A. Savva, D. Moia, M. Zetek, P. R. Barnes, O. G. Reid, S. Inal, G. Rumbles, G. G. Malliaras, J. Nelson, J. Rivnay, I. McCulloch, *Chem. Mater.* **2018**, *30*, 2945.
[3] R. Kroon, D. Kiefer, D. Stegerer, L. Yu, M. Sommer, C. Müller, *Adv. Mater.* **2017**, *29*, 1700930.
[4] J. Liu, L. Qiu, G. Portale, J. C. Hummelen, W. R. Browne, G. ten Brink, B. J. Kooi, L. J. A. Koster, *Adv. Mater.* **2017**, *29*, 1701641.
[5] J. Liu, L. Qiu, R. Alessandri, X. Qiu, G. Portale, J. Dong, W. Talsma, G. Ye, A. A. Sengrian, P. C. T. Souza, M. A. Loi, R. C. Chiechi, S. J. Marrink, J. C. Hummelen, L. J. A. Koster, *Adv. Mater.* **2018**, *30*, 1704630.
[6] J. Rivnay, S. Inal, B. A. Collins, M. Sessolo, E. Stavrinidou, X. Strakosas, C. Tassone, D. M. Delongchamp, G. G. Malliaras, *Nat. Commun.* **2016**, *7*, 11287.
[7] B. Meng, H. Song, X. Chen, Z. Xie, J. Liu, L. Wang, *Macromolecules* **2015**, *48*, 4357.
[8] F. Jahani, S. Torabi, R. C. Chiechi, L. J. A. Koster, J. C. Hummelen, *Chem. Commun.* **2014**, *50*, 10645.
[9] X. Chen, Z. Zhang, Z. Ding, J. Liu, L. Wang, *Angew. Chem. Int. Ed.* **2016**, *55*, 10376.
[10] A. Armin, D. M. Stoltzfus, J. E. Donaghey, A. J. Clulow, R. C. R. Nagiri, P. L. Burn, I. R. Gentle, P. Meredith, *J. Mater. Chem. C* **2017**, *5*, 3736.
[11] S. Rousseva, H. den Besten, F. S. van Kooij, E. L. Doting, N. Y. Doumon, E. Douvogianni, L. J. A. Koster, J. C. Hummelen, *J. Phys. Chem. C* **2020**, *124*, 8633.
[12] L. J. A. Koster, S. E. Shaheen, J. C. Hummelen, *Adv. Energy Mater.* **2012**, *2*, 1246.
[13] S. Torabi, F. Jahani, I. van Severen, C. Kanimozhi, S. Patil, R. W. A. Havenith, R. C. Chiechi, L. Lutsen, D. J. M. Vanderzande, T. J. Cleij, J. C. Hummelen, L. J. A. Koster, *Adv. Funct. Mater.* **2015**, *25*, 150.

[14] J. Brebels, J. V. Manca, L. Lutsen, D. Vanderzande, W. Maes, *J. Mater. Chem. A* **2017**, *5*, 24037.
[15] X. Liu, B. Xie, C. Duan, Z. Wang, B. Fan, K. Zhang, B. Lin, F. J. M. Colberts, W. Ma, R. A. J. Janssen, F. Huang, Y. Cao, *J. Mater. Chem. A* **2018**, *6*, 395.
[16] G. Han, Y. Yi, Z. Shuai, *Adv. Energy Mater.* **2018**, *8*, 1702743.
[17] Y. Olivier, J.-C. Sancho-Garcia, L. Muccioli, G. D'Avino, D. Beljonne, *J. Phys. Chem. Lett.* **2018**, *9*, 6149.
[18] P. Friederich, A. Fediai, S. Kaiser, M. Konrad, N. Jung, W. Wenzel, *Adv. Mater.* **2019**, *31*, 1808256.
[19] T. Wang, G. Kupgan, J.-L. Brédas, *Trends Chem.* **2020**, *2*, 535.
[20] N. R. Tummala, Z. Zheng, S. G. Aziz, V. Coropceanu, J.-L. Brédas, *J. Phys. Chem. Lett.* **2015**, *6*, 3657.
[21] G. D'Avino, Y. Olivier, L. Muccioli, D. Beljonne, *J. Mater. Chem. C* **2016**, *4*, 3747.
[22] S. Sami, P. A. B. Haase, R. Alessandri, R. Broer, R. W. A. Havenith, *J. Phys. Chem. A* **2018**, *122*, 3919.
[23] S. Sami, R. Alessandri, R. Broer, R. W. A. Havenith, *ACS Appl. Mater. Interfaces* **2020**, *12*, 17783.
[24] H. D. de Gier, F. Jahani, R. Broer, J. C. Hummelen, R. W. A. Havenith, *J. Phys. Chem. A* **2016**, *120*, 4664.
[25] A. Ojala, A. Petersen, A. Fuchs, R. Lovrincic, C. Poelking, J. Trollmann, J. Hwang, C. Lennartz, H. Reichelt, H. W. Hoeffken, A. Pucci, P. Erk, T. Kirchartz, F. Wurthner, *Adv. Funct. Mater.* **2012**, *22*, 86.
[26] B. P. Rand, D. Cheyns, K. Vasseur, N. C. Giebink, S. Mothy, Y. Yi, V. Coropceanu, D. Beljonne, J. Cornil, J.-L. Brédas, J. Genoe, *Adv. Funct. Mater.* **2012**, *22*, 2987.
[27] W. Ma, J. R. Tumbleston, M. Wang, E. Gann, F. Huang, H. Ade, *Adv. Energy Mater.* **2013**, *3*, 864.
[28] J. R. Tumbleston, B. A. Collins, L. Yang, A. C. Stuart, E. Gann, W. Ma, W. You, H. Ade, *Nat. Photonics* **2014**, *8*, 385.
[29] C. Poelking, D. Andrienko, *J. Am. Chem. Soc.* **2015**, *137*, 6320.
[30] N. A. Ran, S. Roland, J. A. Love, V. Savikhin, C. J. Takacs, Y.-T. Fu, H. Li, V. Coropceanu, X. Liu, J.-L. Brédas, G. C. Bazan, M. F. Toney, D. Neher, T.-Q. Nguyen, *Nat. Commun.* **2017**, *8*, 79.
[31] C.-K. Lee, C.-W. Pao, *J. Phys. Chem. C* **2014**, *118*, 11224.
[32] J.-M. Y. Carrillo, Z. Seibers, R. Kumar, M. A. Matheson, J. F. Ankner, M. Goswami, K. Bhaskaran-Nair, W. A. Shelton, B. G. Sumpter, S. M. Kilbey, *ACS Nano* **2016**, *10*, 7008.
[33] V. Negi, O. Wodo, J. J. van Franeker, R. A. J. Janssen, P. A. Bobbert, *ACS Appl. Energy Mater.* **2018**, *1*, 725.
[34] D. P. McMahon, D. L. Cheung, A. Troisi, *J. Phys. Chem. Lett.* **2011**, *2*, 2737.
[35] G. D'Avino, S. Mothy, L. Muccioli, C. Zannoni, L. Wang, J. Cornil, D. Beljonne, F. Castet, *J. Phys. Chem. C* **2013**, *117*, 12981.
[36] R. Alessandri, J. J. Uusitalo, A. H. de Vries, R. W. A. Havenith, S. J. Marrink, *J. Am. Chem. Soc.* **2017**, *139*, 3697.
[37] S. J. Marrink, H. J. Risselada, S. Yefimov, D. P. Tieleman, A. H. de Vries, *J. Phys. Chem. B* **2007**, *111*, 7812.
[38] S. J. Marrink, D. P. Tieleman, *Chem. Soc. Rev.* **2013**, *42*, 6801.
[39] T. To, S. Adams, *Phys. Chem. Chem. Phys.* **2014**, *16*, 4653.
[40] A. Wadsworth, Z. Hamid, M. Bidwell, R. S. Ashraf, J. I. Khan, D. H. Anjum, C. Cendra, J. Yan, E. Rezasoltani, A. A. Y. Guilbert, M. Azzouzi, N. Gasparini, J. H. Bannock, D. Baran, H. Wu, J. C. de Mello, C. J. Brabec, A. Salleo, J. Nelson, F. Laquai, I. McCulloch, *Adv. Energy Mater.* **2018**, *8*, 1801001.
[41] R. J. Kline, M. D. McGehee, E. N. Kadnikova, J. Liu, J. M. J. Fréchet, M. F. Toney, *Macromolecules* **2005**, *38*, 3312.
[42] G. J. Hedley, A. Ruseckas, I. D. W. Samuel, *Chem. Rev.* **2017**, *117*, 796.
[43] L. Ye, W. Zhao, S. Li, S. Mukherjee, J. H. Carpenter, O. Awartani, X. Jiao, J. Hou, H. Ade, *Adv. Energy Mater.* **2017**, *7*, 1602000.
[44] M. T. Dang, L. Hirsch, G. Wantz, *Adv. Mater.* **2011**, *23*, 3597.
[45] S. D. Collins, N. A. Ran, M. C. Heiber, T.-Q. Nguyen, *Adv. Energy Mater.* **2017**, *7*, 1602242.
[46] D. Fazzi, M. Barbatti, W. Thiel, *J. Phys. Chem. Lett.* **2017**, *8*, 4727.
[47] K. Vandewal, S. Albrecht, E. T. Hoke, K. R. Graham, J. Widmer, J. D. Douglas, M. Schubert, W. R. Mateker, J. T. Bloking, G. F. Burkhard, A. Sellinger, J. M. J. Frechet, A. Amassian, M. K. Riede, M. D. McGehee, D. Neher, A. Salleo, *Nat. Mater.* **2014**, *13*, 63.
[48] G. Grancini, M. Maiuri, D. Fazzi, A. Petrozza, H. Egelhaaf, D. Brida, G. Cerullo, G. Lanzani, *Nat. Mater.* **2013**, *12*, 29.
[49] K. R. Graham, C. Cabanetos, J. P. Jahnke, M. N. Idso, A. El Labban, G. O. Ngongang Ndjawa, T. Heumueller, K. Vandewal, A. Salleo, B. F. Chmelka, A. Amassian, P. M. Beaujuge, M. D. McGehee, *J. Am. Chem. Soc.* **2014**, *136*, 9608.
[50] T. A. Wassenaar, K. Pluhackova, R. A. Böckmann, S. J. Marrink, D. P. Tieleman, *J. Chem. Theory Comput.* **2014**, *10*, 676.
[51] G. D'Avino, L. Muccioli, F. Castet, C. Poelking, D. Andrienko, Z. G. Soos, J. Cornil, D. Beljonne, *J. Phys. Condens. Matter* **2016**, *28*, 433002.
[52] M. Swart, P. T. van Duijnen, *Mol. Simul.* **2006**, *32*, 471.
[53] P. Kordt, J. J. M. van der Holst, M. Al Helwi, W. Kowalsky, F. May, A. Badinski, C. Lennartz, D. Andrienko, *Adv. Funct. Mater.* **2015**, *25*, 1955.
[54] M. Bouhassoune, S. van Mensfoort, P. Bobbert, R. Coehoorn, *Org. Electron.* **2009**, *10*, 437.
[55] H. van Eersel, R. A. J. Janssen, M. Kemerink, *Adv. Funct. Mater.* **2012**, *22*, 2700.
[56] J. Idé, R. Méreau, L. Ducasse, F. Castet, H. Bock, Y. Olivier, J. Cornil, D. Beljonne, G. D'Avino, O. M. Roscioni, L. Muccioli, C. Zannoni, *J. Am. Chem. Soc.* **2014**, *136*, 2911.
[57] T. M. Burke, S. Sweetnam, K. Vandewal, M. D. McGehee, *Adv. Energy Mater.* **2015**, *5*, 1500123.
[58] S. Zhang, J. Gao, W. Wang, C. Zhan, S. Xiao, Z. Shi, W. You, *ACS Appl. Mater. Inter.* **2018**, *1*, 1276.
[59] B. Xu, X. Yi, T.-Y. Huang, Z. Zheng, J. Zhang, A. Salehi, V. Coropceanu, C. H. Y. Ho, S. R. Marder, M. F. Toney, J.-L. Brédas, F. So, J. R. Reynolds, *Adv. Funct. Mater.* **2018**, *28*, 1803418.
[60] S. Torabi, *Ph.D. Thesis*, University of Groningen, **2018**.
[61] L. Qiu, J. Liu, R. Alessandri, X. Qiu, M. Koopmans, R. W. A. Havenith, S. J. Marrink, R. C. Chiechi, L. J. A. Koster, J. C. Hummelen, *J. Mater. Chem. A* **2017**, *5*, 21234.
[62] F. Grunewald, G. Rossi, A. H. de Vries, S. J. Marrink, L. Monticelli, *J. Phys. Chem. B* **2018**, *122*, 7436.
[63] R. Alessandri, P. C. T. Souza, S. Thallmair, M. N. Melo, A. H. de Vries, S. J. Marrink, *J. Chem. Theory Comput.* **2019**, *15*, 5448.
[64] L. Monticelli, *J. Chem. Theory Comput.* **2012**, *8*, 1370.
[65] C. Oostenbrink, A. Villa, A. E. Mark, W. F. van Gunsteren, *J. Comput. Chem.* **2004**, *25*, 1656.
[66] O. Andreussi, I. G. Prandi, M. Campetella, G. Prampolini, B. Mennucci, *J. Chem. Theory Comput.* **2017**, *13*, 4636.
[67] J.-D. Chai, M. Head-Gordon, *Phys. Chem. Chem. Phys.* **2008**, *10*, 6615.
[68] R. Alessandri, S. Sami, J. Barnoud, A. H. de Vries, S. J. Marrink, R. W. A. Havenith, May **2020**, https://doi.org/10.6084/m9.figshare.5853060.
[69] D. H. de Jong, S. Baoukina, H. I. Ingólfsson, S. J. Marrink, *Comput. Phys. Commun.* **2016**, *199*, 1.
[70] M. J. Abraham, T. Murtola, R. Schulz, S. Páll, J. C. Smith, B. Hess, E. Lindahl, *SoftwareX* **2015**, *1*, 19.
[71] R. Alessandri, S. Sami, J. Barnoud, A. H. de Vries, S. J. Marrink, R. W. A. Havenith, May **2020**, https://10.6084/m9.figshare.12338633.
[72] N. Michaud-Agrawal, E. J. Denning, T. B. Woolf, O. Beckstein, *J. Comput. Chem.* **2011**, *32*, 2319.
[73] R. J. Gowers, M. Linke, J. Barnoud, T. J. E. Reddy, M. N. Melo, S. L. Seyler, D. L. Dotson, J. Domanski, S. Buchoux, I. M. Kenney, O. Beckstein, In *Proc. of the 15th Python in Science Conf., Austin, TX* (Eds: S. Benthall, S. Rostrup), SciPy, **2016**, pp. 102–109, http://conference.scipy.org/proceedings/scipy2016/oliver_beckstein.html.
[74] M. Elstner, D. Porezag, G. Jungnickel, J. Elsner, M. Haugk, T. Frauenheim, S. Suhai, G. Seifert, *Phys. Rev. B* **1998**, *58*, 7260.

[75] C. F. Guerra, J. Snijders, G. te Velde, E. Baerends, *Theor. Chem. Acc.* **1998**, *99*, 391.
[76] G. te Velde, F. M. Bickelhaupt, E. J. Baerends, C. Fonseca Guerra, S. J. A. van Gisbergen, J. G. Snijders, T. Ziegler, *J. Comput. Chem.* **2001**, *22*, 931.
[77] A. F. Oliveira, P. Philipsen, T. Heine, *J. Chem. Theory Comput.* **2015**, *11*, 5209.
[78] G. D'Avino, L. Muccioli, C. Zannoni, D. Beljonne, Z. G. Soos, *J. Chem. Theory Comput.* **2014**, *10*, 4959.
[79] E. A. Silinsh, *Organic Molecular Crystals: Their Electronic States*, Vol. 16, Springer, New York **2012**.
[80] B. T. Thole, *Chem. Phys.* **1981**, *59*, 341.
[81] P. T. Van Duijnen, M. Swart, *J. Phys. Chem. A* **1998**, *102*, 2399.
[82] S. M. Ryno, S. R. Lee, J. S. Sears, C. Risko, J.-L. Brédas, *J. Phys. Chem. C* **2013**, *117*, 13853.
[83] A. V. Marenich, S. V. Jerome, C. J. Cramer, D. G. Truhlar, *J. Chem. Theory Comput.* **2012**, *8*, 527.
[84] F. L. Hirshfeld, *Theor. Chim. Acta* **1977**, *44*, 129.
[85] M. J. Frisch, G. W. Trucks, H. B. Schlegel, G. E. Scuseria, M. A. Robb, J. R. Cheeseman, G. Scalmani, V. Barone, G. A. Petersson, H. Nakatsuji, X. Li, M. Caricato, A. V. Marenich, J. Bloino, B. G. Janesko, R. Gomperts, B. Mennucci, H. P. Hratchian, J. V. Ortiz, A. F. Izmaylov, J. L. Sonnenberg, D. Williams-Young, F. Ding, F. Lipparini, F. Egidi, J. Goings, B. Peng, A. Petrone, T. Henderson, D. Ranasinghe, et al., Gaussian 16, Revision A.03, 2016, http://gaussian.com/citation_a03/, Gaussian Inc. Wallingford CT.
[86] C. Poelking, K. Daoulas, A. Troisi, D. Andrienko, in *Morphology and Charge Transport in P3HT: A Theorist's Perspective*, Springer, Berlin **2014**, pp. 139–180.